Ionized Solid Propellant Rocket Exhaust Plume: MiLES Simulation and Comparison to Experiment

A. Guy[1]*, B. Fromentin-Denozière[2], H-K. Phan[2], A. Cheraly[2], D. Gueyffier[1], V. Rialland[4], C. Erades[1], P.Q. Elias[3], J. Labaune[3], J. Jarrige[3], A. Ristori[1], C. Brossard[1], S. Rommeluere[4]

(1)   ONERA, Multi-Physics for Energetics Department

BP 80100 – 91123 Palaiseau Cedex France, Email: aurelien.guy@onera.fr

(2)   ONERA, Electromagnetism and Radar Department,

BP 80100 – 91123 Palaiseau Cedex France,

(3)   ONERA, Instrumentation and Sensing Department,

BP 80100 – 91123 Palaiseau Cedex France,

(4)   ONERA, Optics and Associated Techniques Department,

BP 80100 – 91123 Palaiseau Cedex France,

An experimental work has been conducted to characterize the properties of a solid rocket motor exhaust plume, culminating in measurement of its electromagnetic properties including radar backscattered spectrum. Reactive MiLES simulations of the plume, including dispersed alumina phase, have been performed on two meshes (8.4 M and 20 M cells) to characterize the plume's turbulence, aerothermochemistry, and ionized structures dynamics.

Experimental images of IR, visible and OH* spontaneous emission have yielded information on the potential core, the mixing layer, and the flame structures, and suggest a flapping mode of the plume's tail. X band phase and transmission measurements have allowed an estimation of the electron density using a 1D model. The role of alkali salts in the ionization process has been confirmed.

MiLES simulations have been processed to study the turbulence development; and to emphasize the strong effect of turbulent dispersion of particles. The flame and ionized structures have been compared to RANS simulations, and electron density is compared to experimental results. Electromagnetic simulations have allowed assessing the reliability of the 1D model used to estimate electron number density. Finally, first estimates of the large structures frequency have been obtained analysing the experimental and numerical data. This will allow analyzing the backscattered radar spectrum.

1. Introduction

Due to specific impulse optimization, a solid rocket motor (SRM) exhaust plume is fuel rich and contains hot H_2, CO and HCl that generate a postcombustion flame when released in ambient air. Alkali species impurities contained in the propellant ingredients (e.g. K, Na) undergo thermal ionization when passing through the recombustion flame, and release electrons. Hence, ionized plumes from solid rocket engines interact with electromagnetic waves. This can result in radio attenuation of signal transmitted between ground and the rocket, which has motivated several works in literature, among which recent work at JAXA [1]. Also, plumes exhibit a radar signature, which can be exploited for radar rocket detection. In this case, the reflected radar wave exhibits a "pseudo-Doppler" spectral broadening, which generates a characteristic radio spectrum, due to the unsteady nature of the plume flow. In this paper, we present an effort to investigate the aerothermochemistry, turbulence, ionization and eventually spectral signature of solid propellant rocket engines, both numerically and experimentally.

On the simulation side, we present an effort to simulate the unsteady behaviour of such a plume through large-eddy simulation. This plume is challenging simulation: firstly it is a

---

* Corresponding author

supersonic turbulent flow. Secondly, the plume undergoes recombustion and ionization, and requires a nonequilibrium chemical kinetics modelling. Finally, the liquid alumina requires a dispersed-phase modelling. To the authors' knowledge, this simulation is the first work including all these phenomena.

A second aspect of this project has been the firing and measurements on several small-scale rocket engines. UHF monostatic radar has been used to measure the plume's backscattered spectrum. As the radar wavelength and the plume size are of the same order of magnitude, this is a very global measurement, and a more refined characterization of the plume, flame and electron field structure has been performed thanks to several additional devices.

In the following, we present a comparison between a RANS simulation, and two MiLES simulations performed on two different meshes. The test case, the physical and numerical models, and the MiLES meshes are presented in the first section. In the second section, we present a comparison between the 2 MiLES and the RANS numerical simulations. Finally, numerical simulations are compared to available experimental data in the third section.

2. Physical and numerical models, and meshes

Test case: firing of MOSER SRM
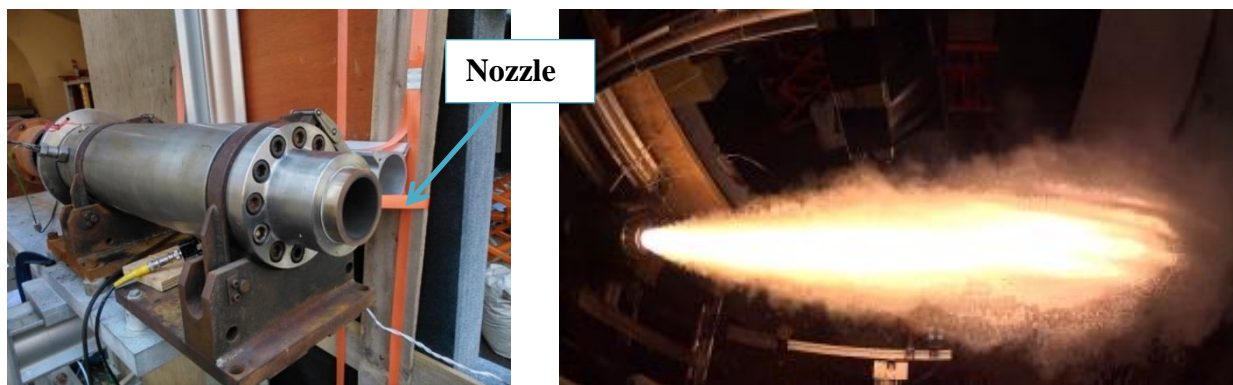
Figure 1 : Picture of the lab-scale MOSER SRM used in the firing campaign (left), photography during the firing (right)

The small scale SRM (Figure 1, roughly 2,000 N thrust) was fired with 8 different star-shaped propellant loadings, including both aluminum free and aluminum containing propellants. The propellants were seeded with various quantities of alkali salts (NaCl and KCl), to quantify their effect on ionization. To precisely control their characteristics, the propellants were built and fired in ONERA. A converging-diverging De Laval graphite nozzle is used, with an area ratio 4.83, 15° half-angle conical divergent, and D = 50 mm nozzle outlet diameter.

The propellant under study is of "Butalane" type, with a 68 % mass percentage of ammonium perchlorate, and 18 % aluminum. It was seeded with potassium containing alkali salts in order to increase ionization in the plume. The motor pressure evolves between 2 MPa and 2.8 MPa during the firing; pressure of 2.25 MPa was retained for the simulations. Photography of the firing taken from an overview camera is shown in Figure 1: the motor nozzle is on the left side, and the flow is directed rightward. The large bright light is the alumina containing postcombustion flame, which is attached to the nozzle exit for this propellant.

Experimental apparatus

The motor was equipped with two sensors to monitor the pressure, and was synchronized with the measurements devices. Figure 2 show the observation ranges of the different devices described hereafter.

Several imagery cameras were positioned to observe a zone between roughly x = 10 cm and x = 1.4 m or x = 2.1 m from the nozzle exit (NE). A 100 Hz band II IR camera with 640*512 resolution and a 2 kHz visible camera with 1024*512 resolution have been used to investigate the plume's structure and dynamics. A UV camera equipped with a spectral filter camera has been used to observe the OH* emission to visualize the heat release zones.

A band II IR spectrometer (2.5-5 µm) has been used to analyse a 10 cm in diameter portion of the plume at x = 90 cm from the NE. X-band attenuation and phase-shift were measured using a network analyzer 80 cm from the NE, to estimate the electron density and collision frequency. Finally, monostatic UHF band radar positioned with and angle of 60 ° from the plume axis was used to measure the radar spectral energy density backscattered by the plume.
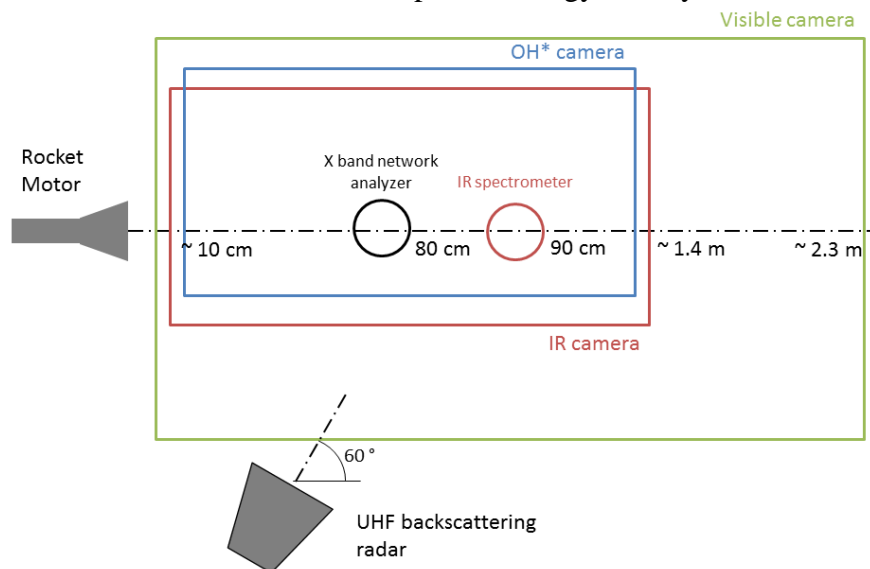
Figure 2 : Implantation of measure devices

Chamber conditions

ONERA's thermodynamic and rocket performance code COPPELIA [18] is used to compute the thermodynamic equilibrium composition of the gases resulting from the propellant combustion inside the engine, at fixed pressure and enthalpy. It also computes performance of the rocket engine using a quasi-1D nozzle expansion. The alkalis are included into the gaseous phase, and equilibrium composition is computed, resulting in an ionization fraction of about 10^{-6} in the motor chamber. The composition is given in Table 1, for the chamber pressure 22.5 bar.

Species	Mass fraction	Mole fraction	Species	Mass fraction	Mole fraction
Cl	0.02398019	1.2204E-02	O	0.00048685	5.4900E-04
Cl_2	0.0000516	1.3130E-05	O_2	0.00012251	6.9075E-05
CO	0.40277784	2.5944E-01	OH	0.00662231	7.0252E-03
CO_2	0.02559533	1.0493E-02	e^-	0	8.7335E-07
H	0.00266915	4.7776E-02	Cl^-	0.00006134	3.1215E-05
H_2	0.03803906	3.4044E-01	K	0.00002453	1.1318E-05

H_2O	0.1101366	1.1030E-01	K^+	0.00006954	3.2089E-05
HCl	0.2604736	1.2889E-01	KCl	0.00070555	1.7074E-04
N_2	0.128184	8.2557E-02			

Table 1: Equilibrium composition of the burnt propellant gases

Performance parameters and RANS simulation results have been used to compute the plume characteristics parameters and nondimensional numbers, which are given in Table 2. The relatively low Reynolds number is due to the high kinematic viscosity of hot plume gases at the nozzle outlet. The relatively low Mach number on the axis is due to the alumina phase drag. A RANS calculation with a low-Reynolds mesh and k-w SST model [19] has allowed computing the boundary layer properties. The displacement thickness is $\delta^* = 0.38$ mm, and the momentum thickness is $\theta = 0.093$ mm (using the compressible definition), which yields the shape factor given in the table. The plume is slightly overexpanded.

Mach number	*1.75 (axis) – 2.3 (max)*	P_{ch}	*22.5 bar*
Reynolds number	*290 000 (exhaust gases properties)*	T_{ch}	*3325 K*
U / D convective time for Strouhal number	*40 kHz*	$T_{nozzle\ outlet}$	*2400 K (axis)*
H (boundary layer shape factor)	*2.97 (incompressible), 4.08 (compressible)*	P_e / P_{atm}	*0.8*
$\rho_{alumina} / \rho_{gaz}$ *(alumina mass loading)*	*0.31*	T_{ch} / T_{atm}	*11*

Table 2: Characteristics and nondimensional numbers describing the exhaust plume

CEDRE code

CEDRE is ONERA's multi-physics simulation code, designed to solve multiphase, chemically reacting, supersonic flows coupled to radiation transfer, film deposition on walls, and heat conduction in solids [2]. It solves flows on general unstructured meshes, and used a parallel approach based on domain decomposition. In particular, it is used for exhaust plume simulation for infrared signature simulation [3] and radar signature simulation [4] using a customized k-ε turbulence modeling. Also, it has been used for several years to perform large-eddy simulations of jet engine [5] and rocket engine [6] plumes for aeroacoustics applications, which inherently require time-dependent simulations.

Gas phase flow modeling

Gas phase is simulated with CEDRE's CHARME solver. HLLC shock-capturing scheme, with 2nd order accurate spatial multislope reconstruction along with an in-house "hybrid" slope limiter (ref. [10]) is used to compute the convective fluxes.

When the MiLES approach is used, i.e. the turbulent stresses, species diffusion and heat conduction are not modeled and are assumed to be implicitly represented by the numerical scheme. The 2D axisymmetric RANS simulations are performed using a k-ε turbulence model, with constants modified for axisymmetric supersonic mixing layers [11], with constant turbulent Schmidt and Prandtl numbers equal to 0.9. Laminar transport is based on mass gradient-driven laminar diffusion, Fourier's law, and Sutherland viscosity law, and species dependent Prandtl and Schmidt numbers.

Temporal integration is performed using a 2nd order implicit Runge-Kutta method. The maximum CFL number in the simulation domain is about 2.5 for both simulations, the timestep being 1.25×10^{-7} s. The total CPU time for performing the LES simulations is 2 million CPU hours.

Chemical kinetics model

ONERA's kinetic scheme for recombustion in SRM exhaust plumes, designed to deal with chlorine containing exhaust gases [8] has been used. It involves 12 species and 17 chemical reactions. Laminar reaction rates have been used.

To represent potassium ionization, we used 5 extra species, with a chemical kinetics scheme adapted from the kinetic scheme of Jensen and Jones [9].

Two-phase flow modeling

The dispersed phase is modeled using an Eulerian approach which involves solving mass, momentum and energy equations. In the simulation, the dispersed phase is assumed to be characterized by only one particle diameter calculated using Hermsen correlation [7], $d_p = 3.5$ μm. Dispersed phase is coupled to the gaseous phase in a two-way manner, using classic drag and heat flux coefficients for particles.

Alumina is assumed to be liquid in the whole plume, with a density 2890 kg/m^3, a specific heat capacity 1888 J/K/kg. We assume that particles are spherical, do not rotate, and have uniform temperature.

Godunov type scheme are used for convective fluxes, with 2nd order accurate spatial reconstruction with an in-house "hybrid" slope limiter, associated to multislope reconstruction (cf. ref. [10]).

Simulation domain and boundary conditions

The simulation domain is shown on Figure 3. Boundaries are set far enough from the plume, and mesh is coarsened when approaching them, to dampen most reflected acoustic waves. Propellant decomposition products are injected upstream the nozzle convergent portion, assuming a uniform flow profile in the section. In particular, no noise is introduced in the simulation. Alumina particles are injected assuming thermal and mechanical equilibrium with the gas phase in the injection section. Adiabatic and no-slip conditions are used for all walls. To speed-up the transient phase in the simulations, an air co-flow of 298 K air at 20 m/s is imposed on the left and lateral boundaries, whereas atmospheric pressure is imposed at the right boundary.
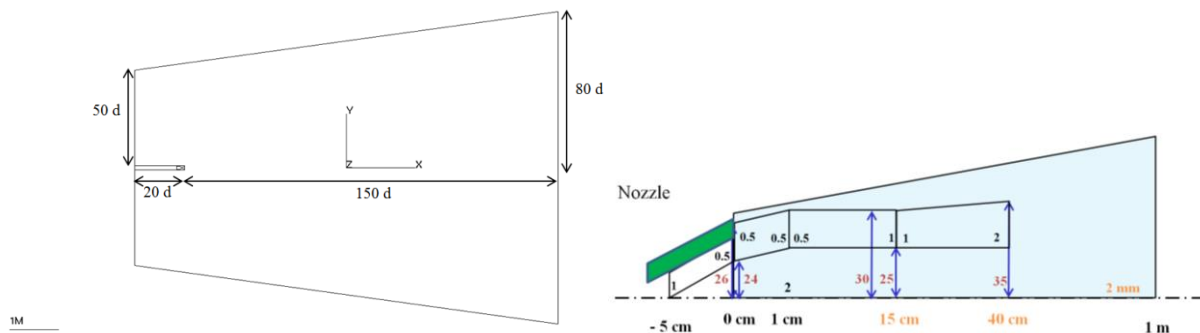
Figure 3 : Simulation domain (left), and mesh resolution zones used for the fine (20 M) mesh. The green shape represents the nozzle divergent section

Meshes characteristics
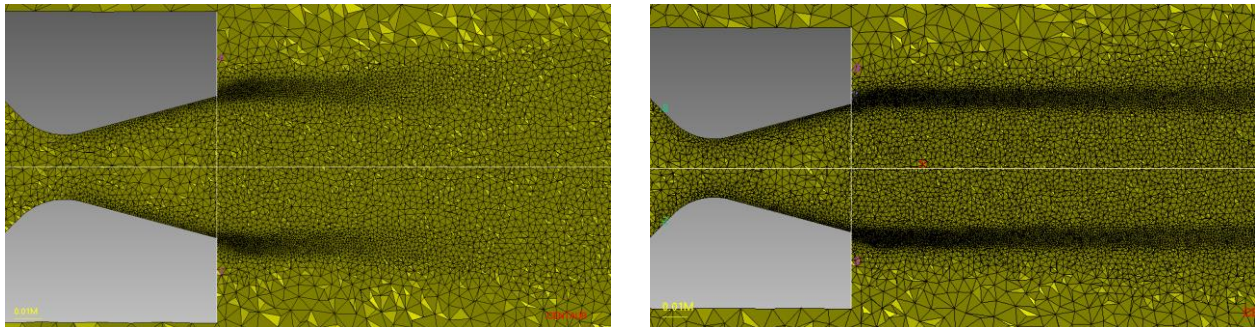
Figure 4: Zoom near the nozzle exit on a cut view to show the grid cell size for the 8.4 M) (left) and the 20 M (right) grids

3D unstructured meshes used in MiLES calculations were created using the CENTAUR Software. Meshes are mainly composed of tetrahedrons. Domain size and refinement criterion between adjacent cells have been carefully chosen to avoid spurious acoustic reflections. Mesh size is specified by using geometrical refinement zones, mainly of the "frustrum" type. Two meshes have been successively designed, a first "coarse" 8.4 million cells mesh, and a second "fine" 20 million cells mesh, that can be seen on Figure 4. The refinement zones used for the 20 M are presented on Figure 3. There are 314 cells 0.5 mm large in the azimuthal direction at the nozzle outlet. In the wake of the nozzle lip, resolution is slowly relaxed and reaches 1 mm 3 D (3 nozzle diameters, i.e. 15 cm) downstream the nozzle outlet (1 D for the 8.4 M grid), and reaches 2 mm 8 D from the nozzle outlet (2 D for the 8.4 M grid). Elsewhere in the englobing zone extending up to the first 20 D from the nozzle outlet, resolution is 2 mm for the 20 M mesh and 4.2 mm for the 8.4 M mesh.

2D axisymmetric unstructured mesh is used for RANS simulation. It is designed to use a wall law approach, and is composed of about 41,000 cells.

Simulation procedure and post-processing

A first coarse mesh was used to establish the plume with recombustion. The solution was then projected on both the 8.4 M and the 20 M mesh, where it was advanced until statistical convergence was achieved. Then, the simulation was run during 20 ms (800 D/U convective times) for the 8.4 M mesh and during 17.25 ms (690 D /U) for the 20 M mesh. Simulations were run on 1,024 CPUs and the total CPU time was 2 million hours.
3D snapshots of electron density and collision frequency fields were recorded every D/U. Time-averaged 3D fields were obtained for both meshes. Then, azimuthal averages of these fields were performed to yield smooth 2D axisymmetric flow fields discussed hereafter.

3. Numerical results comparison

Turbulence development in the mixing layer
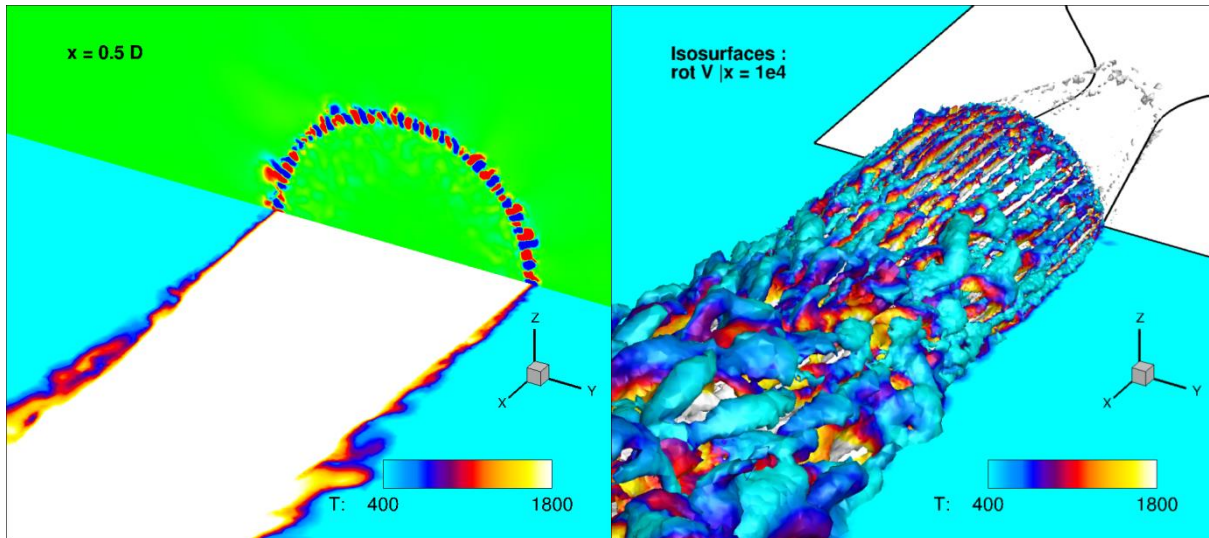
Figure 5 : Cut plane showing axial vorticity sign (red and blue) at x = 0.5 D from the nozzle exit (left). Isosurface of axial vorticity (10^{-4} s^{-1}) colored by temperature obtained on a snapshot on 20 M mesh (right)

As illustrated on Figure 5, a manifold of longitudinal Görtler-like vortices is obtained in the simulations. The first flow fluctuations seem to appear at the location where these vortices merge. This has been observed in at least 2 other LES supersonic jet simulations performed at ONERA with finer mesh resolution. It would be interesting to see whether such structures are observed in DNS computations, or in some experiments (such as ref. [16]), as the mesh at the nozzle wall is of course far from being fine enough to reliably capture the turbulence development.
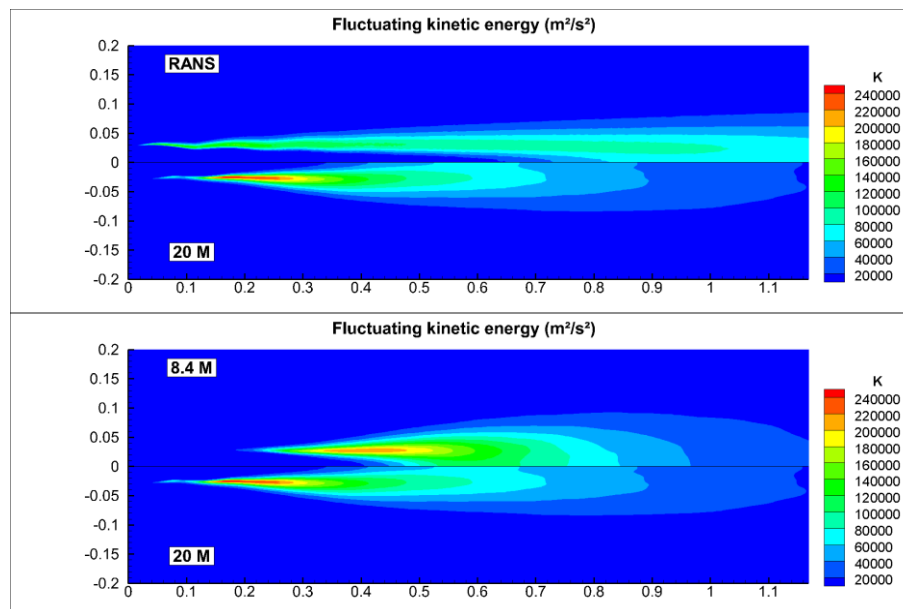
Figure 6 : Comparison between the map of turbulent kinetic energy computed using the RANS approach, and the fluctuating kinetic energy computed from the LES approach on the 8.4 M and 20 M grids (time and azimuth average)

In Figure 6, turbulent and fluctuant kinetic energy obtained with RANS and LES (time and azimuth average) calculations are compared. In RANS, we observe earlier turbulence

development, but lower energy levels are attained. In LES, the finer grid leads to an earlier turbulence development.

A more quantitative analysis is provided by Figure 7 (left): following Troutt and McLaughlin [12], the maximum level of fluctuating velocity (normalized by the nozzle exit velocity) in the mixing layer is plotted along the plume. The above conclusions are confirmed, and the fluctuation level reaches 14.5 % 1D from the NE in the RANS simulation. The effect of mesh refinement between 1 D and 3 D is obvious in the LES simulations. A peak of fluctuation is observed just downstream the first shock cell (1 D), in accordance with the experimental observations of André et al. [13] on the modulation of turbulence by shock structures in underexpanded jets. Contrary to what is observed by these authors on cold air jets, the turbulence level is not constant, especially in the LES simulations. It should be investigated whether this results from a simulation biais, or from the effect of the postcombustion flame.

In Figure 7 (right) are plotted the axial evolution of the mixing layer position $y_{0.5}$, and thickness, defined as:

- $\delta = y_{0.95} - y_{0.05}$
- $y_{0.05}$ is the position where $\|\vec{V}\|(y_{0.05}) = 0.05 * (\|\vec{V}\|_{co-flow} - \|\vec{V}\|_{max})$

The evolution of δ with the RANS calculation is linear, which is typical of a jet with a fully turbulent boundary layer as experimentally observed by Troutt and McLaughlin [12], and André et al.[13]. However, the evolutions obtained with the LES simulations are more indicative of a partly laminar mixing layer. In this figure, we observe that refining of the beginning of the mixing layer up to 3 D has dramatically improved this point in the refined zone. After that, the linear character is lost, and the mixing layer thickens faster. An interesting definition of the potential core length arises as the intersection point between the 2 curves: the 20 M jet is a shorter than the 8.4 M jet and the RANS jet.
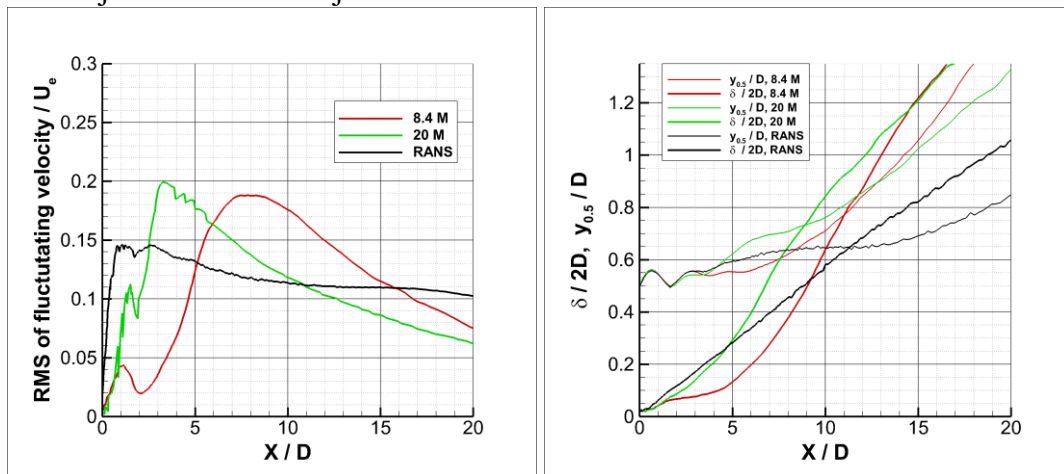
Figure 7 : Comparison between the axial evolutions of the RMS fluctuating velocity maximum value in the plane transverse to the axis (left). Comparison of the axial evolution of the shear layer position $y_{0.5}$ and thickness δ. RANS approach (black), LES approach on the 8.4 M and 20 M grids (time and azimuth averages)

To complete this turbulence analysis, Figure 8 shows the power spectral density (PSD) $E_1(k_x)$ of axial velocity on axis at x = 10 D and x = 20 D from the nozzle exit, for the 20 M mesh. The FFTs are computed using the Hanning window, and smoothed using the Welch method.

At x = 10 D, turbulence is largely developed, which is consistent with the end of the potential core being situated upstream (at x = 9 D in this calculation). There is indeed a zone where the $St^{-5/3}$ universal law is approximately fulfilled. At St = 1, the mesh cut-off frequency is largely exceeded, hence the fall of spectral energy density. A peak near St = 0.2 (i.e. 8 kHz) is observed on the smoothed PSD, as well as numerous peaks for example at St = 0.025 (1 kHz) and

St = 0.45 (1.8 kHz). Significant energy is present in the low frequency range; however, longer time sample would be desirable to improve the statistics.

At x = 20 D, turbulence is still fully developed, and turbulent kinetic energy is lower. The peak near St = 0.45 (1.8 kHz) has become more prominent.

Finally, it is worth noting that the PSD is performed at punctual locations. It would be interesting to associate the obtained frequencies to the main dynamics structures of the plume; this goal could be attained via a POD (proper orthogonal decomposition) analysis.
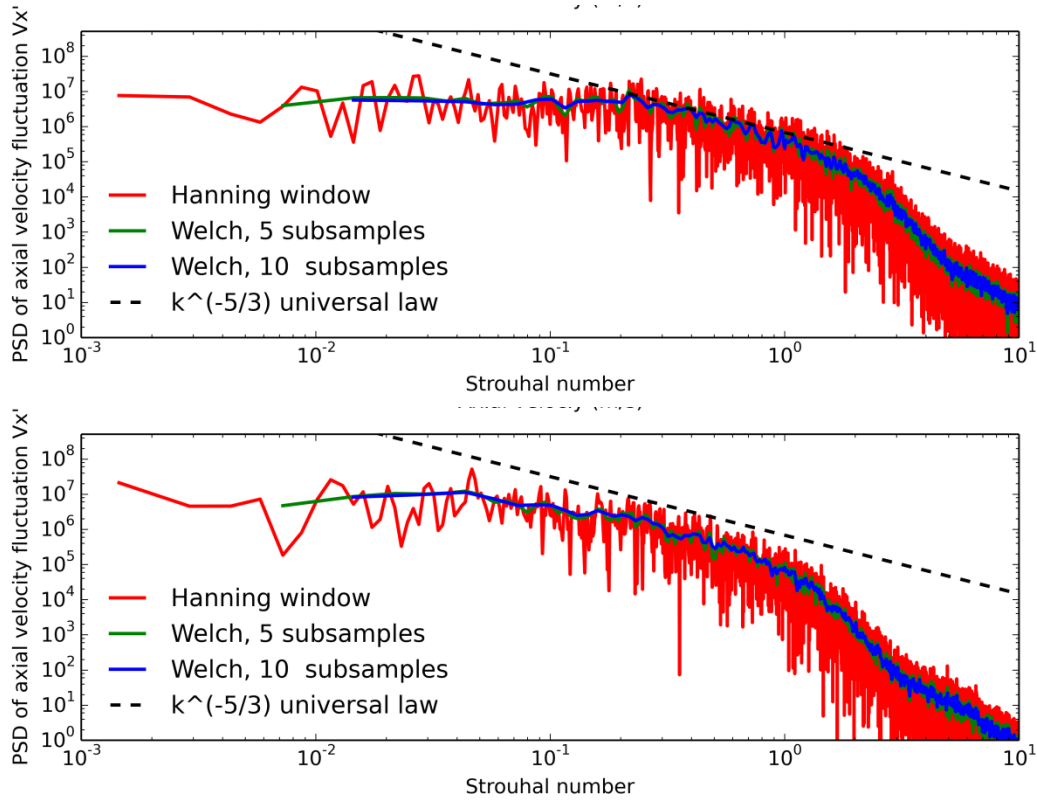
Figure 8 : Power spectral density of fluctuating axial velocity (m²/s²/Hz) on axis, at x = 0.5 m = 10 D (top) and at x = 1 m = 20 D (bottom) from the nozzle exit, for the 20 M mesh

To finish with, Table 3 gives the position of the first shock x_1, the length of the first shock cell L_1, the length of the sonic core L_s and the length of the potential core L_{pot}, along with values obtained from literature correlations. The LES jets are shorter than the RANS jet, but the order of magnitude is good.

	RANS	LES 8.4 M	LES 20 M	Correlations
x_1	0.05 m	0.05 m	0.05 m	-
L_1	0.105 m	0.105 m	0.105 m	0.15 m (Eldred [14], M_j = 2.3, D_j ~ 0.05 m)
L_S	1.1 m	0.73 m	0.75 m	0.72 – 1.36 m, 1.86 m (Nagamatsu Horvay [15], M_e = 1.6-2.3, M_e = 2.7, D_e = 0.05 m)
L_{pot}	0.56 m	0.55 m	0.44 m	0.61 m (Eldred, M_j = 2.3, D_j ~ 0.05 m)

Table 3: Comparison of some plume characteristics to literature correlations for the 3 simulations

Combustion

Figure 9 shows the Abel transform of the heat release rate w_T. The first thing that these figures show is a substantial difference between the RANS flame, which reaches it maximum intensity on the beginning of the mixing layer, whereas the LES flames reach their maximum intensities at the end of the potential core. As for the aerodynamics, the most intense part of the flame is shorter on the 20 M mesh than on the 8.4 M mesh. However, the length based on 25 % of the maximum range is about the same for both LES simulations. Despite the large cell size difference (2 mm vs. 4.2 mm at the end of the potential core), the flame structure is relatively similar in both LES simulations.
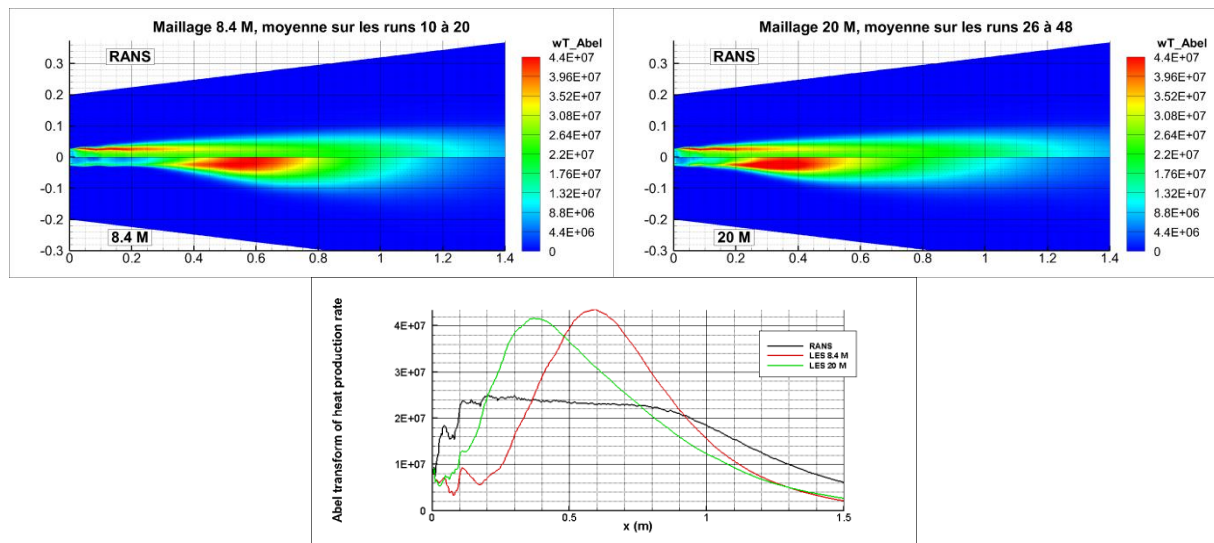
Figure 9 : Abel transform of the heat production rate (time and azimuth averaged) for the RANS and LES simulation. Map (top) and axial evolution on the axis (bottom)

Two-phase flow effects

The same gas/particle interaction models are used in RANS and LES simulation. Though, Figure 10 exhibits dramatically different results: whereas RANS particle spray remains focused, LES particle spray is dispersed by large turbulent structures. This leads to an order of magnitude difference on the particle volume fraction on the axis, 1 meter from nozzle exit. Considering the high alumina mass loading, this can have important impact on the jet temperature and momentum.

Noise levels observed on the LES results come from the fact that only a few snapshots of particles field could be stored and used for the time average, which was not at that time computed for the dispersed phase. Aside this post-processing issue, a good agreement is observed between the two LES simulations, despite the finer structures captured by the 20 M mesh, as shown in

Figure 11. In the Stokes regime, the particle relaxation time would be $\tau_p = \frac{\rho_p d_p^2}{18\mu_g} \sim 2.10^{-5}\ s$, which would indicate an interaction of the particles with turbulent structures up to St ~ 1. Comparison of PSD of axial velocity between both meshes shows an increase of PSD after St ~ 0.5 when the mesh is refined. This is consistent with a limited effect of the finer structures resolved on the particles.
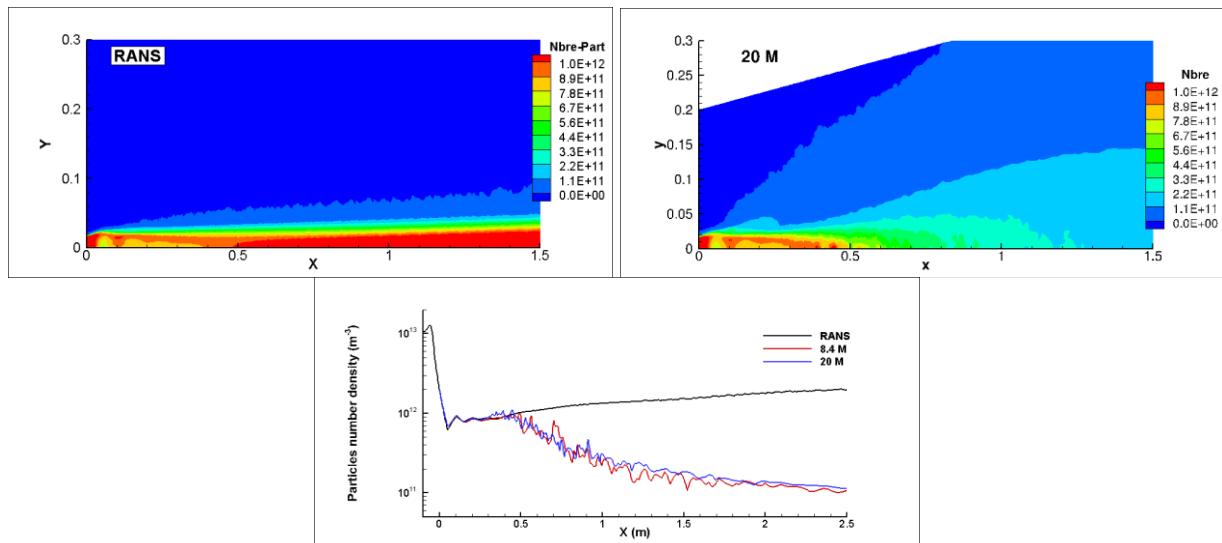
Figure 10 : Alumina particles number density maps for the RANS (top left) and LES simulation (top right, time and azimuth averaged). Axial evolution for the 3 simulations (bottom)
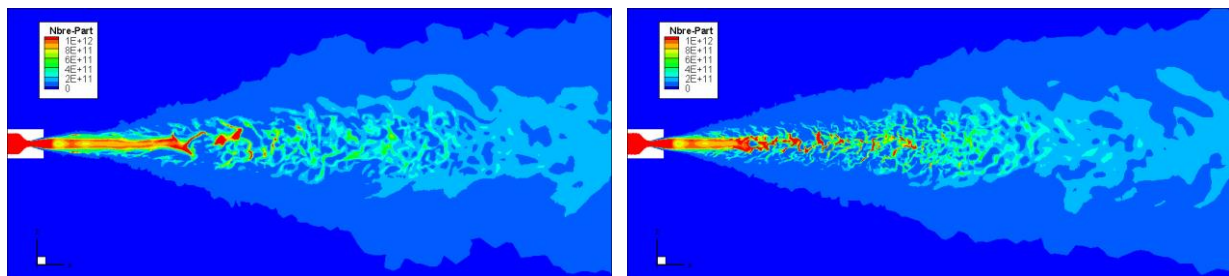
Figure 11 : Snapshot of a cut-view of alumina particles number density maps for the 8.4 M LES simulation (left) and for the 20 M LES simulation (right)

Electron density maps

Figure 12 shows the mean electron density maps. Two types of high electron density zones are observed: in the potential core behind the shock waves, and in the mixing zones, undergoing combustion. The potential core is similar between all simulations, but the mixing zones have different shapes, and the maximum electron densities exhibit (moderate) differences, these zones being thicker and shorter in LES simulations. It is also shown than the electron density standard variation is large, being about 50 % of the mean electron density.

The Abel transform of electron density on the axis is provided to give an estimation of the total electron content seen by the X band measurements: at x = 80 cm, noticeable differences exist between the simulation results. Again, the LES plumes are shorter than the RANS one, also from the electron density point of view.
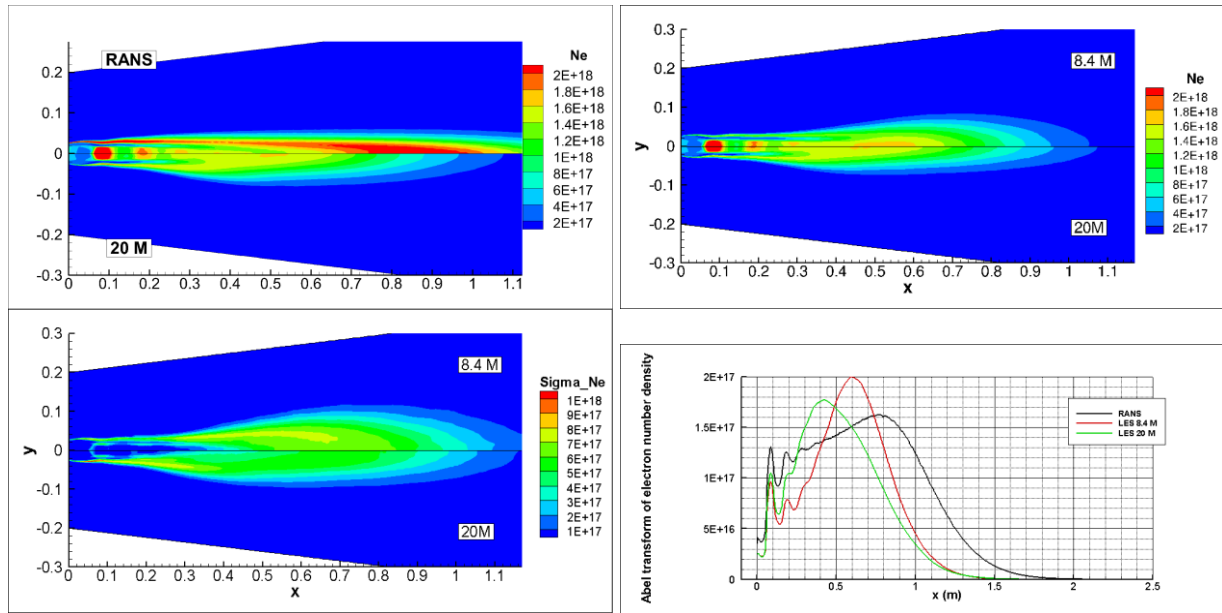
Figure 12 : Top: Mean value of electron number density computed with RANS approach and with LES approach on 8.4 M and 20 M grids (time and azimuthal average).
Bottom: standard deviation of electron number density, and Abel transform of electron number density, on the axis

The snapshots shown in Figure 13 indicate large unsteadiness and inhomogeneity of the time-dependent electron fields. Large structures still exist on the on the finer grid, but finer structures appear as well. This suggests that still finer structures should exist on the experimental plume.
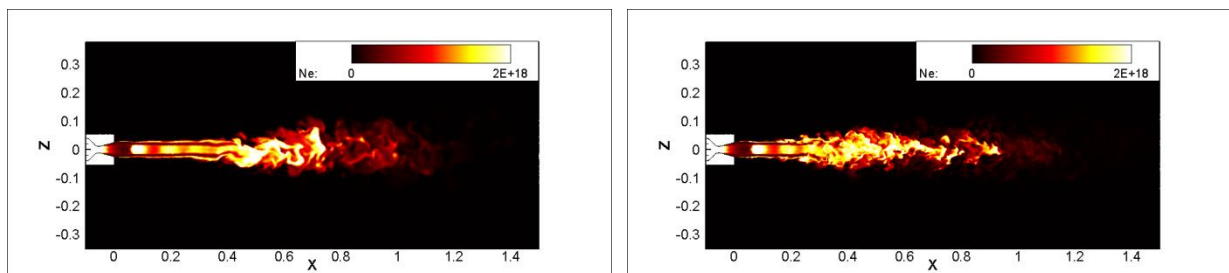
Figure 13 : Snapshots of electron number density computed with LES on 8.4 M (left) and 20 M (right) grids

Largely unsteady and inhomogeneous ionized structures lead to large electron density variation, as shown by the PDF in Figure 14 which shows 3 orders of magnitude variations in N_e, 1m from the nozzle exit.
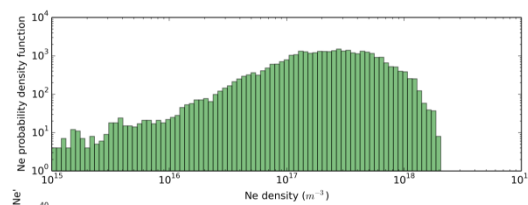
Figure 14 : PDF of electron density at x = 1 m from the NE (20 D), for the 20 M mesh. Mean value : 3.1e17 m^{-3}, RMS value : 2.7e17 m^{-3}

3. Comparison to experimental measurements

Gas and particles: µSPOC spectrometer

ONERA's high-speed IR spectrometer µSPOC was positioned to observe a 10 cm diameter zone located at x = 90 cm from the nozzle exit. Contrary to some other firings with less energetic propellants where postcombustion was absent (not shown here), gaseous species (especially molecular) radiation dominates aver particles/soot radiation at this location.

This supports the theory that alumina particles have been dispersed, as suggested by the LES computations. IR radiation transfer simulations will allow examining further this assumption.
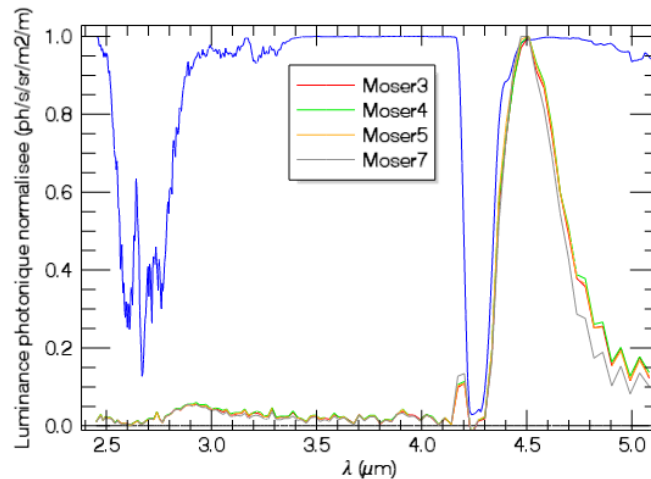
Figure 15 : Spectral luminance (arbitrary units) measured using the µSPOC medium-speed spectrometer, located 0.9 m from the nozzle exit on the plume axis, for several firings. The blue line corresponds to the atmosphere transmissivity

Shock structures: IR camera

Figure 16 and Figure 17 show experimental data acquired with IR camera using several µs of exposure time at a 100 Hz framerate. The images allow a clear vision of the potential jet structures. It is interesting to note that the shock structures seem quite smooth. On the IR figures, the jet seems of constant thickness: about 5 cm in diameter (green contour). We also observe a 2 cm in diameter brighter zone (red contour), that corresponds to the hot, particle loaded, core jet.

On the presented snapshot, a flapping mode is clearly evidenced. Using the profile 19 in Figure 17, the wavelength of this oscillation is estimated to be about 40 cm. The RANS simulation results indicate that the axial velocity is between 700 and 1000 m/s at these locations. If we assume it to result from the convection of a structure, we can provide a first estimate its frequency: $f_{flap} = \frac{850 \; m.s^{-1}}{0.4 \; m} \sim 2 \; kHz$. Note that this structure is found only on a few snapshots: it appears to be intermittent.
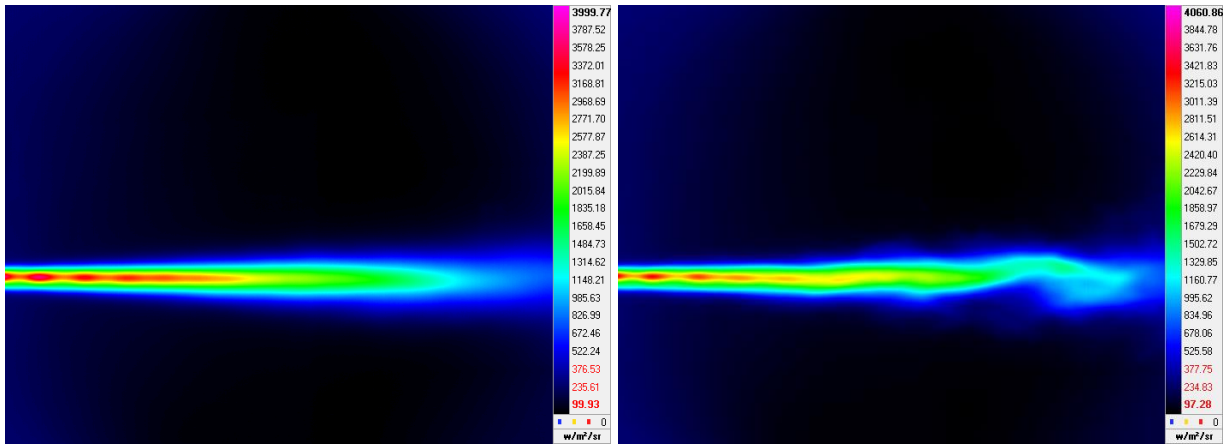
Figure 16 : Infrared time averaged (left) and snapshot (right) images obtained with a band 2 IR camera.
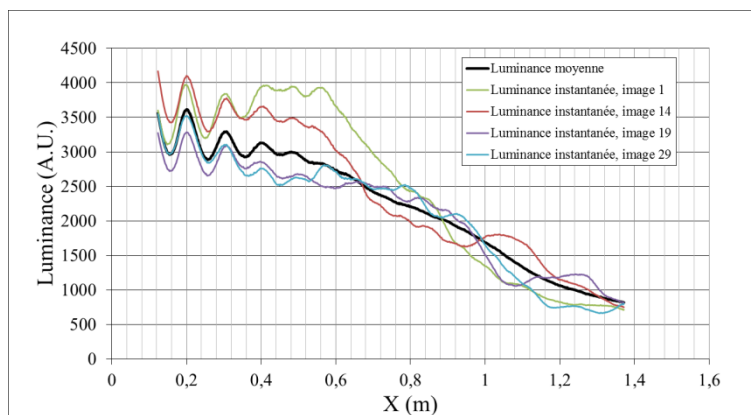
Figure 17 : Axial evolution of infrared signal for time average (black) and several snapshots (colors) corresponding to chamber pressures between 22bar and 23 bar

Visible camera

Mean intensity image in Figure 18 shows that the core structure of the jet can also be observed using a visible camera, however with less accuracy on the shock patterns than for the IR images. The opening of the plume, associated with the mixing layer, can also be observed. In particular, the standard deviation figure exhibit a clear, luminous frontier, that seems to correspond to the mixing layer limit at least up to 1m from the nozzle exit. The mixing layer boundaries defined by $y_{0.95}$ coming from the 3 simulations have been superimposed on the images.

The maximal standard deviation zone (10 % of max intensity in the plume) between 1 m and 1.6 m of the NE, and is indirectly linked to the flame oscillations. An important part of the visible radiation may come from hot particles radiation: one possible interpretation could be that the standard deviation corresponds to the particles passing through flames puffs.

When looking at some couples of consecutive images obtained using visible camera (not shown here), 2 phase-opposed flappings are observed: this suggests a ~ 2 kHz flapping. However, the camera framerate is insufficient to ascertain this conclusion.
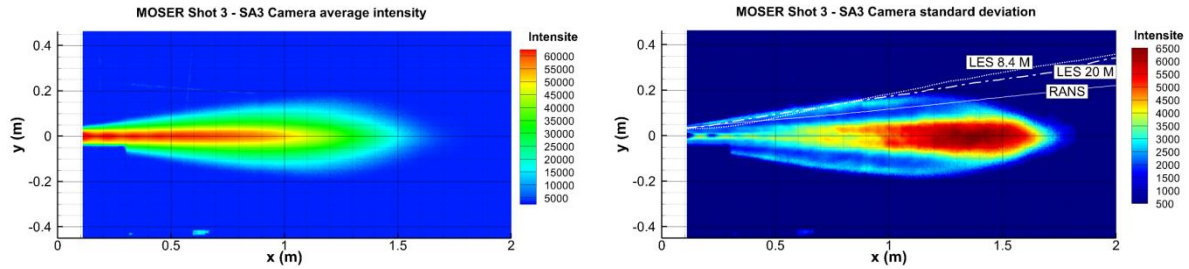
Figure 18 : Mean (top) and standard deviation of intensity obtained with the visible camera

Combustion: OH* camera
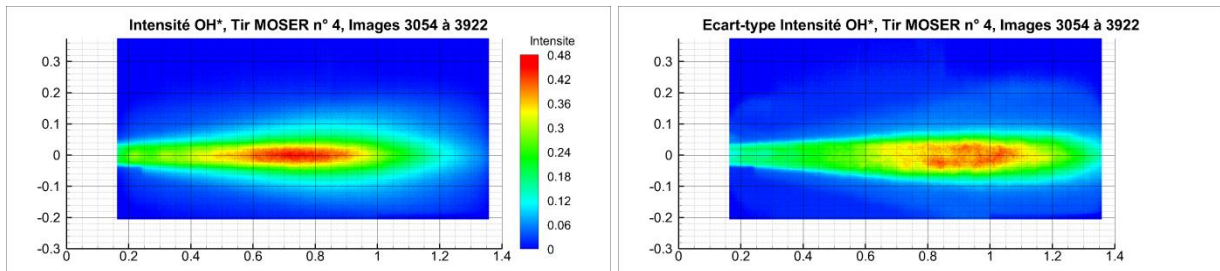
Figure 19 : Intensity map average and standard deviation obtained with camera equipped with an OH* filter (arbitrary units). Average on the range of chamber pressures from 22 to 23 bar

Figure 19 shows the mean and standard deviation intensity images obtained with the OH* camera. The mean intensity figure shows a 6 cm in diameter for brightest zone, extending from 0.5 m to 1.05 m. Another color map would clearly show that the flame is holded to the nozzle. Significant emission also comes from the mixing layer. The maximum standard deviation zone extends from 0.6 m to 1.2 m, which is different from the results in the visible range. As OH* emission is associated to the combustion induced heat production rate, these zones correspond to the most energetic intermittent flames.

Imagery comparison

Figure 20 shows a comparison of the axial profiles of IR, visible and OH* intensity. One can conclude that both visible and IR camera evidence the potential core, even if IR gives a better resolution of the shock cells. Then the IR signal decreases faster than the visible signal, even in the zone of strong OH* signal, i.e. the flame zone. As shown by the spectrometer, particles radiation is minor at this location in the IR range. This supports the assumption that particles have been dispersed, because if not, they should have been heated by the flame and strongly radiate.
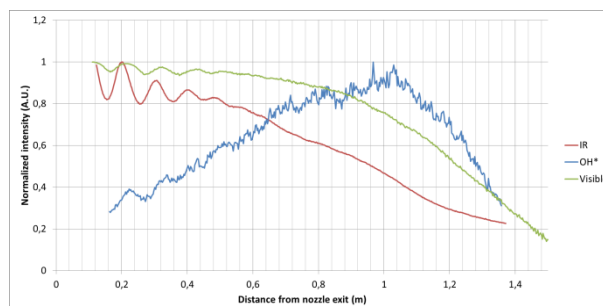
Figure 20 : Axial profile of intensity obtained during firing n ° 3 with IR and visible cameras and during firing n ° 4 with OH* camera

A. Guy et al.

Ionization: X-band measurements

X band measurements aim at estimating the parameters used by the electromagnetic propagation model, i.e. the electron density N_e and the electron-heavy particles collision frequency ν_c in the plume. Signal transmission and phase shift through the plume was measured for several firings. During this campaign, it was undoubtedly observed that plumes emanating from motor with no alkaline impurities, but same propellant composition, had a much lower impact on microwave signals.

An example result is provided in Figure 21. From these measurements at several frequencies, one extract values for N_e = 3-7 x 10^{17} m^{-3} and ν_c = 170 - 470 GHz, assuming a homogenous 10 cm plasma slab model. This has already been performed in literature [17], but is known to sometimes provide approximate results because refraction and diffraction effect should be accounted for.
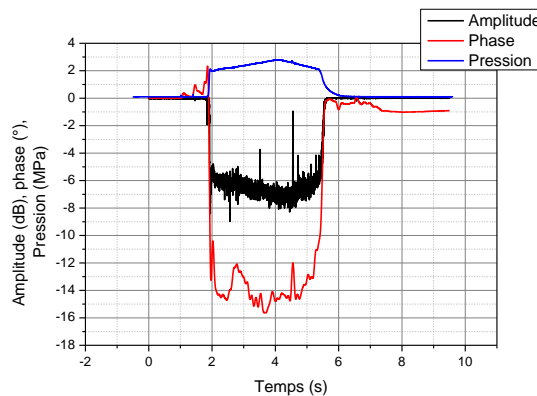
Figure 21 : Pressure, transmitted signal and phase-shift evolution during one motor firing

In order to strengthen the analysis, radial electron density profiles have been extracted (see Figure 22). RANS and average LES profile indicate that 10 cm is a good approximation for the plasma slab thickness. However, the snapshots show that the ionized structures are far from being stationary and homogenous. Thus significant diffraction and refraction effects should alter the results. Moreover, the real plume may exhibit even smaller structure, as LES structures size are limited by the mesh resolution. Conversely, the collision frequency is almost constant.
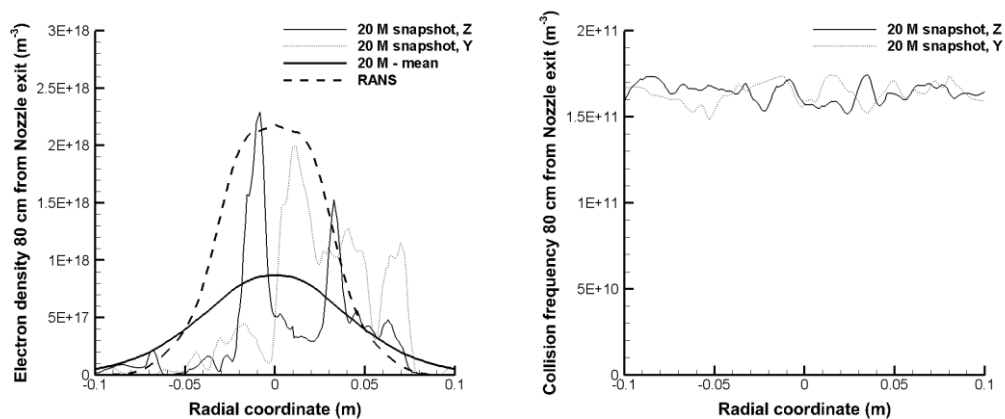
Figure 22 : Left: Radial profile of electron density at x = 80 cm from the NE obtained from RANS, mean and snapshot LES results (along Y and Z axis for the snapshot).Right : radial profile of collision frequency from the LES snapshot

On-going work will allow quantifying for non-1D effects through X band EM (electromagnetic) simulation through 3D plume snapshots. Figure 23 shows a typical computation of the electric

16

field amplitude and phase distribution in a plane behind an axisymmetric SRM (different from the one under study) plume, using a RANS approach. Even for the rather slab-like profiles provided by RANS simulations, significant spatial variation of amplitude and phase are predicted. Work will be continued to characterize these effects for the firing under investigation using both RANS and LES profiles, and provide uncertainty margins.
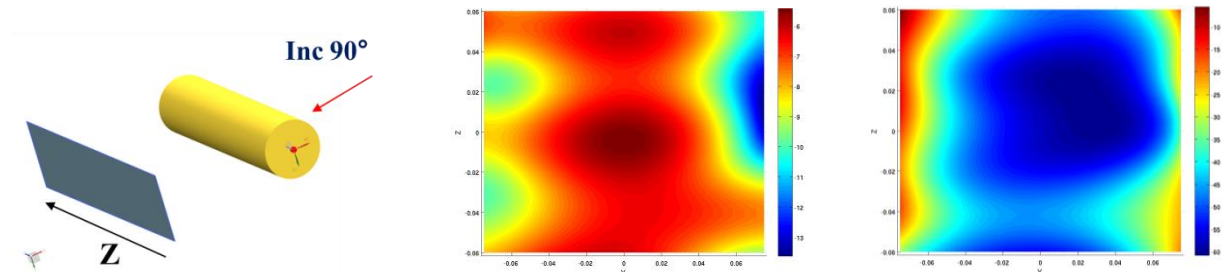
Figure 23 : Intensity attenuation (in dB, middle) and phase shift (in degrees, right) in the entrance plane of the receptor horn

Radar measurements

The final goal of the present campaign is now rapidly discussed. Though the EM simulation of the current firing is still progressing, Figure 24 shows a backscattered radar spectrum simulated from a preliminary study on a coarse LES mesh, and for a non-aluminized propellant. One can observe several bands: one exhibiting no frequency shift, and 3 exhibiting negative frequency shifts up to 1.5 kHz. A significant effect of the aspect angle is also evidenced. Links between the frequency shift and the frequency of the main plume oscillating structures, in particular the postulated flapping mode discussed above, requires further investigation.
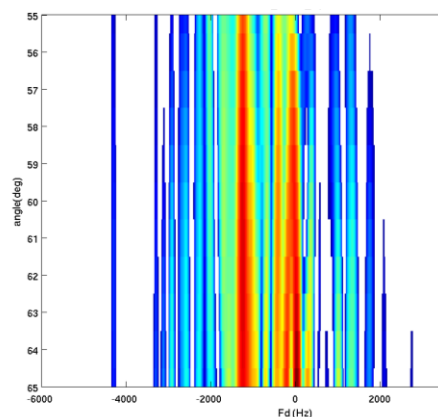
Figure 24 : Simulation of radar spectrum backscattered by another propellant

Conclusions

RANS and MiLES simulations of an alkali containing aluminized propellant have been performed and analyzed. Turbulence transition in the calculation seems to occur through Goertler-like streamwise vortices development and merging; grid dependence and experimental reality of this behavior should be further investigated. Strong particles turbulent dispersion has been observed in MiLES calculations. Study of the particle size effect would be an interesting complement. Comparison of the two MiLES simulations with different meshes evidences an effect of sub-cell physics, even though the qualitative structure remains similar. In particular, it

would be interesting to better describe the effect of micro-mixing between air and hot gases on combustion. MiLES simulations give different flame and ionized structures shape compared to RANS simulations. MiLES simulations also give access to unsteady structures. A peak of fluctuating axial velocity at St ~ 0.45, i.e. f = 1.8 kHz has been obtained at x = 1 m from the nozzle exit. Further investigations should be undergone to determine whether this frequency is representative of a large structure, e.g. a flapping or helical mode.

Preliminary spectrum simulation made on a coarse mesh and different propellant exhibited a strong band around 1.4 kHz. Electromagnetic spectrum simulation using results of the MiLES simulation presented in this work will allow completing the conclusions.

Experimental measurements have been performed:

- IR spectrometer shows dominating contribution of hot gases in the IR band II range at x = 0.9 m from the nozzle exit. The opposite behavior was observed for plumes without recombustion obtained on less energetic propellants, where soot radiation dominates.
- IR camera shows very well the hot core, and an almost constant apparent jet radius. It has revealed an intermittent oscillatory structure of about 40 cm spatial wavelength of the jet plume. A frequency of about 2 kHz has been roughly estimated and should be verified.
- Visible range camera shows hot core of the jet, plus the mixing layer. On standard deviation figure, a limit of the plume is especially well evidenced.
- OH* camera does not show the potential core, but emphasizes the average and fluctuating combustion zones.
- Electron number density and collision frequency are determined from X-band measurements assuming a homogeneous 10 cm plasma slab (1D model). Simulated electron densities are a bit higher than measurements in LES simulations, and 3 times higher in RANS simulation. However, the widely used 1D model is shown to be of limited applicability in this zone. Indeed, as the ionized structures size is smaller than the wavelength, significant refraction and diffraction effects must be accounted for.
- Attenuation measured on the same propellant without alkali impurities inclusion was much lower, demonstrating the used ionization mechanism.

Future work will focus on a more accurate analysis of the large structure shape and frequencies in the simulation. IR simulation using LES results could emphasize any jet tail oscillation, and POD analysis could yield the exact shape and frequency of a large-scale oscillation, including the flapping mode. The radar spectrum simulations will be compared to experimental data, and to the simulated large structure frequencies. This will allow to assess the ability of MiLES simulation to predict the largest ionized structures shape and frequency.

Acknowledgements

References

[1] K. Kinefuchi, K. Okita, I. Funaki, T. Abe, *Prediction of In-Flight Radio Frequency Attenuation by a Rocket Plume*, Journal of Spacecraft and Rockets 52(2), 2015

[2] P. Chevalier, B. Courbet, D. Dutoya, P. Klotz, E. Ruiz, J. Troyes, and P. Villedieu, *CEDRE : development and validation of a mulitphysic computational software*, 1st European conference for aerospace sciences, 2005

[3] V. Rialland, A. Guy, D. Gueyffier, P. Perez, A. Roblin and T. Smithson, *Infrared signature modelling of a rocket jet plume - comparison with flight measurements*, Journal of Physics : Conference Series 676, 2016

[4] D. Gueyffier, B. Fromentin-Denoziere, J. Simon, A. Merlen and V. Giovangigli, *Numerical Simulation of Ionized Rocket Plumes*, Journal of Thermophysics and Heat Transfer 28, 2014

[5] M. Lorteau, F. Clero, F. Vuillot, *Analysis of noise radiation mechanisms in hot subsonic jet from a validated large eddy simulation solutio*n, Journal of Fluid Mechanics 27, 2015

[6] Jean-Baptiste Dargaud, *Simulation numérique de l'onde de souffle et du bruit de jet au décollage d'un lanceur*, PhD Thesis, Université Pierre et Marie Curie – Paris VI, 2013

[7] P.W. Hermsen, *Aluminum Oxide Particle Size for Solid Rocket Motor Performance Evaluation*, Journal of Spacecraft and Rockets 18(6), 1981

[8] J. Troyes, I. Dubois, V. Borie, A. Boischot, *Multi-phase reactive numerical simulations of a model solid rocket motor exhaust jet*, AIAA 2006-4414, 2006

[9] D.E. Jensen, G.A. Jones, *Reaction Rate Coefficients for Flame Calculations*, Combustion and Flame 32, 1978

[10] C. LeTouze, A. Murrone, H. Guillard, *Multislope MUSCL method for general unstructured meshes*, Journal of Computational Physics284, 2015

[11] G. Turpin, J. Troyes, *Validation of a two-equation turbulence model for axisymmetric reacting and non-reacting flows*, 36th AIAA/ASME/SAE/ASEE Joint Propulsion Conference & Exhibit, 2000

[12] T.R. Troutt, D.K. McLaughlin, *Experiments on the flow and acoustic properties of a moderate-Reynolds-number supersonic jet*, Journal of Fluid Mechanics 116, 1982

[13] B. André, T. Castelain, C. Bailly, *Investigation of the mixing layer of underexpanded supersonic jets by particle image velocimetry*, International Journal of Heat and Fluid Flows 50, 2014

[14] K.M. Eldred, *Acoustic loads generated by the propulsion system*, NASA-SP-8072, 1971

[15] H.T. Nagamatsu, G. Horvay, *Supersonic Jet Noise*, 8th AIAA Aerospace Sciences Meeting, AIAA 1970-237, 1970

[16] A. Krothapalli, G. Buzyna, and L. Lourenco, *Streamwise vortices in an underexpanded axisymmetric jet*, Physics of Fluids 3, 1991

[17] Kiyoshi Kinefuchi, Ikkoh Funaki, Toru Shimada, Takashi Abe, *Investigation on Microwave Interference in Full-Scale Solid Rocket Exhaust*, Journal of Spacecraft and Rockets 47 (4), 2010

[18] B. Bourasseau, *Programme de calcul des performances des systèmes propulsifs COPPELIA, 1ère partie : description théorique*, ONERA internal report, 1986

[19] F.R. Menter, *Zonal two-equation k_omega turbulence models for aerodynamic flows*, AIAA Paper 1993-2906, 1993